doi: 10.5028/jatm.2011.03027510

Tiago Cavalcanti Rolim*
Instituto de Estudos Avançados
São José dos Campos /SP – Brazil
tiagorolim@ieav.cta.br

Paulo Gilberto de Paula Toro
Instituto de Estudos Avançados
São José dos Campos/SP – Brazil
toro@ieav.cta.br

Marco Antonio Sala Minucci
Instituto de Estudos Avançados
São José dos Campos/SP – Brazil
sala@ieav.cta.br

Antônio de Carlos de Oliveira
Instituto de Estudos Avançados
São José dos Campos/SP – Brazil
acoc@ieav.cta.br

Roberto da Cunha Follador
Instituto de Estudos Avançados
São José dos Campos/SP – Brazil
follador@ieav.cta.br

*author for correspondence

Experimental results of a Mach 10 conical-flow derived waverider to 14-X hypersonic aerospace vehicle

Abstract: *This paper presents a research in the development of the 14-X hypersonic airspace vehicle at Institute for Advanced Studies (IEAv) from Department of Science and Aerospace Technology (DCTA) of the Brazilian Air Force (FAB). The 14-X project objective is to develop a higher efficient satellite launch alternative, using a Supersonic Combustion Ramjet (SCRAMJET) engine and waverider aerodynamics. For this development, the waverider technology is under investigation in Prof. Henry T. Nagamatsu Aerothermodynamics and Hypersonics Laboratory (LHTN), in IEAv/DCTA. The investigation has been conducted through ground test campaigns in Hypersonic Shock Tunnel T3. The 14-X Waverider Vehicle characteristic was verified in shock tunnel T3 where surface static pressures and pitot pressure for Mach number 10 were measured and, using Schlieren photographs Diagnostic Method, it was possible to identify a leading-edge attached shock wave in 14-X lower surface.*

Keywords: *Hypersonics, Hypersonic systems, Shock tunnel, Schlieren, Waverider.*

INTRODUCTION

A waverider vehicle could be defined as a supersonic or a hypersonic vehicle which uses a leading-edge attached shock wave to form a high pressure zone on its lower surface to generate lift. The interest in hypersonic waverider vehicles lies on the promise of a high lift-to-drag ratio vehicle able to deploy a payload into earth orbit. Until now, research has shown that a waverider vehicle has superior aerodynamic performance compared with other hypersonic aerodynamic concepts as accelerators and as aerogravity-assisted maneuvering vehicles (Rault, 1994). They are also being considered for high-speed long-range cruise vehicles, since their high lift-to-drag ratio becomes important in achieving global range. Furthermore, with horizontal takeoff and landing capability, they could reduce the turn around time of the current space missions. A waverider which uses air breathing propulsion would not need to carry the oxidizer, which results in weight saving, reduced complexity, and less ground support (Javaid, et al., 2005).

A strong candidate for hypersonic propulsion is the Hydrogen fueled scramjet engine. That is because this air breathing engine cycle is capable to provide the thrust required for a hypersonic vehicle more efficiently than conventional rocket propulsion. As a matter of fact, at hypersonic speeds, a typical value for the specific impulse of a H_2-O_2 rocket engine is about 400 s while for a H_2 fueled scramjet is between 2,000 s and 3,000 s (Heiser, et al., 1994). In fact, the use of atmospheric air as oxidizer permits air breathing vehicles to substantially increase payload weight (Figs. 1 and 2).

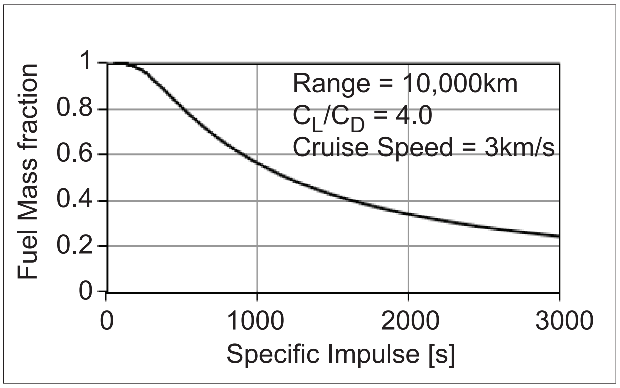

Figure 1. Fuel mass fraction variation with specific impulse (I_{sp}) using Breguet equations for a hypersonic cruise mission.

The waverider's concept was introduced by Terence Nonweiler (Nonweiler, 1963), as a delta shaped reentry vehicle. This concept was named caret shaped waverider

---

Received: 14/06/10
Accepted: 11/07/11

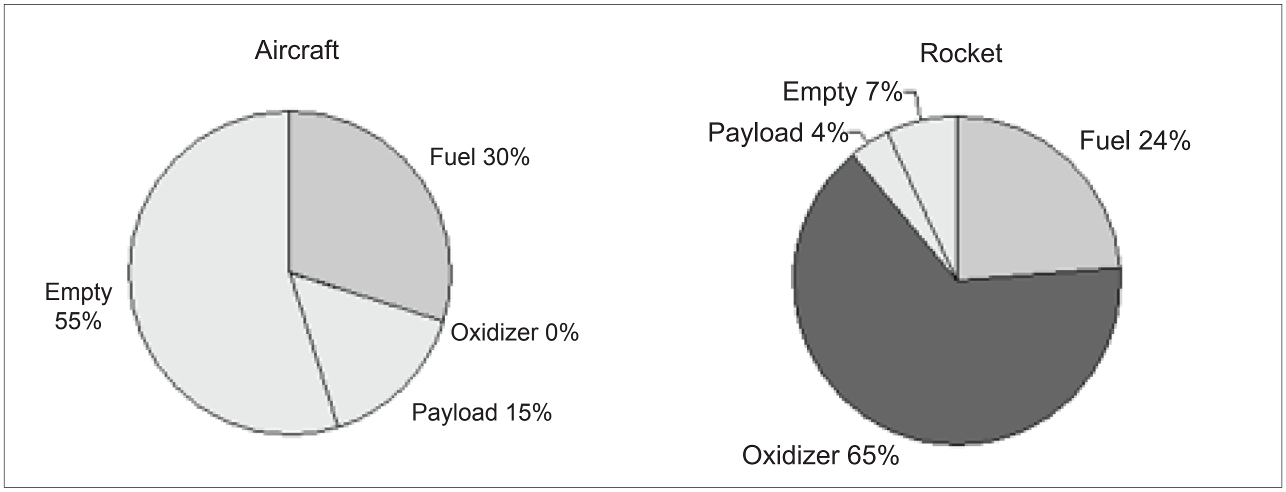

Figure 2. Typical takeoff mass fractions for current aircrafts and rockets, based on data given by Heiser (Heiser, et al., 1994).

due to its resemblance with the typographic symbol (^). While studying the flow over the vehicle, Nonweiler realized that the high pressure on the under surface due to a shock wave could be used for generating lift. Also, the attached shock wave in a sharp leading edge isolates the high pressure zone from the low pressure zone, which inhibits the flow spillage.

Regarding the aerodynamic design of a waverider, its surface is constructed from a base body. The streamlines of the flow over a body are traced to generate the lower surface. The upper surface is generally aligned with the free stream flow. In general, the goal of each method of construction is to attain high values of the lift-to-drag ratio as well as a high package's capacity. Several works regarding the waverider construction, engine integration and geometric optimization have been carried on during recent years.

An important work on waverider design area was performed by Rasmussen (Rasmussen, et al., 1990), which presented an aerodynamic surface that used the shock wave to generate lift. It was derived from a supersonic flow past a cone. The Rasmussen's surface obtained a superior overall performance to the classical Nonweiler's waverider. Since then, various families of cone derived waveriders as well as their hybrid variations like cone-wedge and multiple cone derived waveriders have been studied. The objectives of these studies have been mainly to increase the low lift-to-drag ratio due to viscous effects and to improve the package capability of such vehicles (Wang, et al., 2007; Kim, et al., 1983).

The focus of the analysis described in this work was to investigate the flow field over a waverider derived from a Mach 10 conical flowfield, as described by Rasmussen (Rasmussen, et al., 1990). Also, in order to better assess the engine integration, to the pure waverider surface, a compression ramp, a flat and an expansion surface were added, in order to simulate a scramjet. To improve the efficiency of these engines, the flow must be two-dimensional and uniform, and must have adequate pressure and temperature for the supersonic combustion. Furthermore, the inlet must be large enough so as to generate thrust even in high altitudes, where there's a low air density. To simulate a free expansion nozzle, a 15^{o}-ramp was integrated on the rear of the model.

Thirteen shock tunnel tests were conducted to acquire experimental data for the hypersonic flow over a waverider vehicle's compression surface and the scramjet combustor inlet at high Mach numbers and high total enthalpies. The main goals of the research were: i) to design and build a waverider model with instrumentation; ii) to measure surface static pressures and Pitot pressure for Mach number 10 with high reservoir enthalpies; iii) to take schlieren photographs to support data analysis.

MODEL DESIGN

a) Pure waverider surface

For the present investigation, the waverider model was built according to the Rasmussen method. In that work, the hypersonic small disturbance theory was applied to analyze waveriders derived from axisymmetric flows past circular cones.

As stated above, the design was based on a known flow field over a conical body. Figure 3 shows many parameters of the applied method. Given a conical body (the basic body) and a parabolic upper surface trailing edge, the supersonic flow streamlines are traced back until they reach the shock wave formed by the base body. The generated curve is the vehicle's leading edge. The localization of the leading edge then permits the flow stream lines to be traced downward defining the lower surface trailing edge. Finally, the lower and upper trailing edges along with the leading edge were used to calculate the entire lower surface; the upper surface was aligned to the free stream flow.

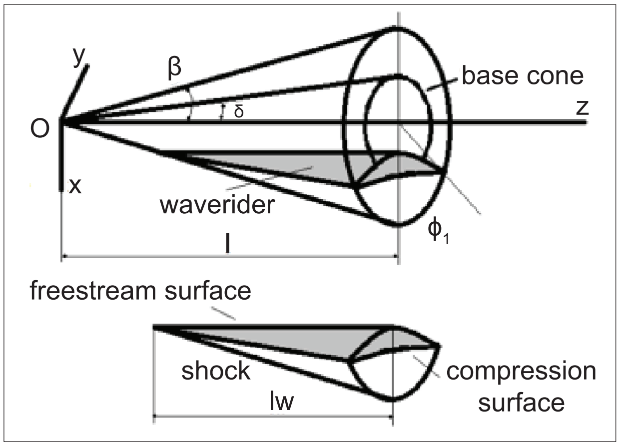

Figure 3: Construction of a general cone-derived waverider (Rasmussen, et al., 1990).

Let us assume a slender cone subjected to a steady inviscid supersonic flow. For this analysis, a spherical coordinate system (r,θ,□) was applied, with origin in the cone vertex (Fig. 3). The free stream velocity V_∞ points in the positive z direction.

In the scheme presented in Fig. 3, the necessary parameters to describe a waverider are: the free stream Mach number M_∞, the ratio of specific heats γ, the semi-vertex cone angle δ, the semi-vertex shock angle β, the dihedral angle $\square_\iota$ and the base body length ι.

For slender cones, the shock wave angle can be calculated with the relation:

$$\frac{\beta}{\delta} = \left(\frac{\gamma + 1}{2} + \frac{1}{M_\infty^2 \delta^2}\right)^{\frac{1}{2}} \tag{1}$$

It is also important to define the three surfaces that are used to describe the waverider: the free stream surface (upper surface), the compression surface (lower surface) and the base plane (z=l).

For small angles, the free stream surface is defined by:

$$r \cdot \theta = r_s(\phi) \cdot \beta \tag{2}$$

where r_s (□) defines the conical shock (θ=β), the intersection of the upper and lower surface, which is also the leading edge.

Similarly, the compression surface is defined by:

$$r \cdot (\theta^2 - \delta^2)^{\frac{1}{2}} = r_s(\phi) \cdot (\beta^2 - \delta^2)^{\frac{1}{2}} \tag{3}$$

Also, since we assume that the upper surface is aligned to the free stream, we just need the upper trailing edge to define the entire upper surface.

In this work, the upper trailing edge was assumed as a parabola, described in Cartesian coordinates in the base plane by:

$$X = R_0 + AY^2 \tag{4}$$

where

A and R_0 are constants;

X = x/ιδ;

Y = y/ ιδ.

Since, at the shock we have: $X=X_s$ and $Y=Y_s$. Thus,

$$A = \frac{X_s - R_0}{Y_s^2} \tag{5}$$

where

$$X_s = \sigma \cos \phi_l \tag{6}$$

$$Y_s = \sigma \sin \phi_l \tag{7}$$

And σ = β/δ.

From the coordinate system analysis, the radial distance projected in the base plane is given by $R_b = r \sin \theta_b$. For small angles, $Rb \approx r\,\theta_b$ and $z = r \cos \theta \approx r$. In the base plane, z=l. Thus, one can define the dimensionless distance of a point in the free stream trailing edge from the axis center projected in the base plane as $R_{\infty b} = \theta_{\infty b}$ (□)/δ. In a similar fashion, for the compression surface, R_{cb}(□) = θ_{cb} (□)/δ .

Using Eqs. 2 and 3 we can relate the compression surface trailing edge with the free stream trailing edge as following:

$$\left(\frac{\theta_{cb}}{\delta}\right)^2 = 1 + \frac{\sigma^2 - 1}{\sigma^2}\left(\frac{\theta_{\infty b}}{\delta}\right)^2 \tag{8}$$

Moreover, it was shown that $\theta_{\infty b}$ is single valued for $0.5 \leq \frac{R_o}{X_s} \leq 1$ (Rasmussen, et al., 1990).

The Hypersonic Small Disturbances Theory permit us to write the lift coefficient as:

$$C_L = \frac{l^2}{S_p}\frac{\delta^2\sigma^3}{\sigma^2-1}\int_0^{\phi_l}\left[1-\frac{R_{cb}(\phi)}{\sigma}\right]cos\phi\, d\phi \qquad (9)$$

Similarly, the drag coefficient can be written as the sum of the pressure drag and the friction drag:

$$C_D = \frac{D_p + D_f}{q_\infty S_p} = C_{D_p} + C_f\frac{S_w}{S_p} \qquad (10)$$

where S_p and S_w are the waverider plan form and wetted areas, respectively. With $q_\infty = \frac{1}{2}\rho_\infty V_\infty^2$ and,

$$C_{D_p} = \frac{l^2}{S_p}\frac{\delta^4\sigma^2}{\sigma^2-1}\int_0^{\phi_l}\left[1-\frac{R_{cb}^2}{\sigma^2}-\ln\left(\frac{R_{cb}^2}{\sigma^2}\right)\right]d\phi \qquad (11)$$

The friction drag coefficient was evaluated based on a laminar flow, thus:

$$C_f = \frac{0.664F_0F_1}{\sqrt{Re_{l_w}}} \qquad (12)$$

where

$$Re_{l_w} = \frac{\rho_\infty V_\infty l_w}{\mu_\infty} \qquad (13)$$

and

$$F_0 = \frac{4l^2\delta}{S_{w\infty}}\left(\frac{l_w}{l}\right)^{\frac{1}{2}}\int_0^{\phi_l}\left[1-\frac{R_{\infty b}}{\sigma}\right]^{\frac{1}{2}}\left[R_{\infty b}^2+\left(\frac{dR_{\infty b}}{d\phi}\right)^2\right]^{\frac{1}{2}}d\phi \qquad (14)$$

$$F_1 = \frac{S_{w\infty} + (1+\gamma M_\infty^2\delta^2)^{\frac{1}{2}}S_{wc}}{S_w} \qquad (15$$

The design involved a tradeoff analysis in order to find the dihedral angle □ι and the base cone angle δ that would maximize the lift-to-drag ratio $\frac{C_L}{C_D}$ and the volumetric efficiency $V^{\frac{2}{3}}/S_p$. This analysis is summarized in Figs. 4 and 5. It must be pointed out that our design option was $M_\infty = 10$. Moreover, since $0.5 \leq \frac{R_o}{X_s} \leq 1$ we chose $R_0/X_s = 0.75$. In fact, examining Eqs. 4 and 5 one can see that low values of R_0/X_s could result in final geometries with excessive bluntness and, ultimately, large drag. On the other hand, values of R_0/X_s close to 1 produce very slender geometries.

As a general result, for a fixed δ, the lift-to-drag ratio is maximum near 30° this behavior is depicted in Fig. 4, for δ = 5.5°. On the other hand, the volumetric efficiency was minimum at 37° but from □ι = 20° to 50° its variation was irrelevant, less than 5%.

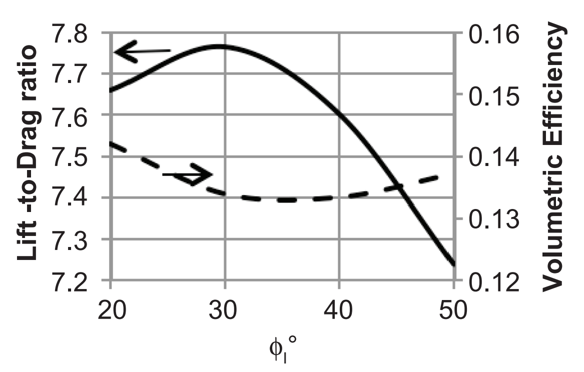

Figure 4. Effect of the dihedral angle on the waverider characteristics, with δ = 5.5°.

Furthermore, the influence of the base cone angle δ was investigated (Fig. 5). One can conclude that the lift-to-drag ratio is maximum at 5.5°, and it varies slightly over the considered range of δ. Also, the volumetric efficiency is significantly improved as δ increases. Although a large volumetric efficiency is desired, the drag increases with δ^2, as shown in Fig. 6. Thus, to avoid the drag penalty to a large volumetric efficiency, and maximize the lift-to-drag ratio, we chose δ = 5.5°. and □ι = 30°. The final configuration is shown in Fig. 7.

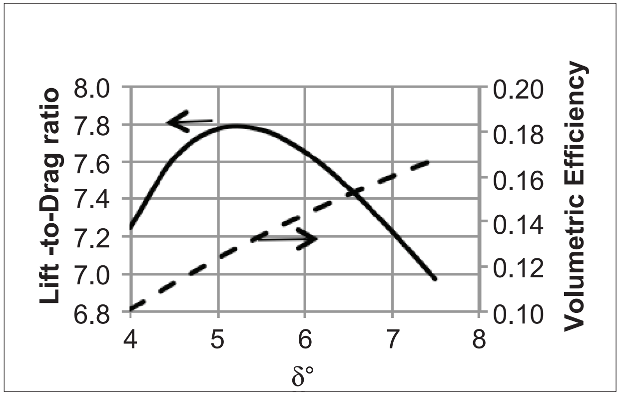

Figure 5. Effect of the base cone angle on the waverider characteristics, with φι = 30°.

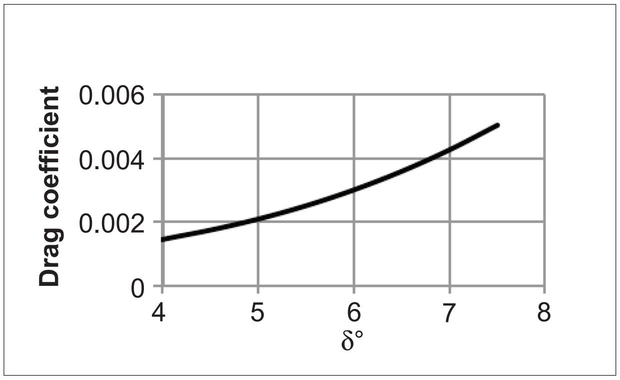

Figure 6. Drag coefficient for several base cone angles, with □ι = 30° .

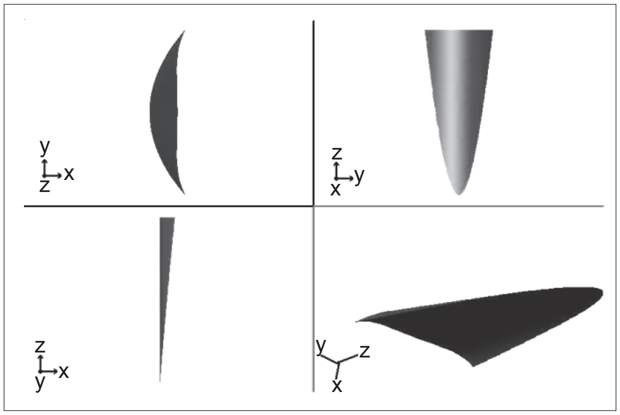

Figure 7. Generated waverider, for □ = 30°, M = 10, δ = 5.5° and R_o/X_s = 0.75.

b) Scramjet inlet

The design goal of the compression system is to provide the desired pressure and temperature for the supersonic combustion over the entire flight range with minimum losses.

Bearing this fact in mind, one must consider that after the conical shock wave produced by the leading edge and after the compression ramp, the flow must reach the adequate conditions, or close to them, for autoignition of the Hydrogen-Air mixture, pressures between 25-100kPa and temperatures between 1000-2000K (O'neill, et al., 1992). Furthermore, due to the fact that a hypersonic waverider in this study would be used for transatmospheric missions, the change of the air properties with flight altitude must be accounted, this was used to define the limits for the scramjet operation in the present analysis.

The inlet ramp adopted was a single turn ramp. Also, two-dimensional, calorically perfect and inviscid flow, were assumed in that region. These assumptions substantially simplify calculations for the ramp geometry to be matter of investigation. Figure 8 shows the flow schematics, the free stream flow is compressed by the forebody which produces a conical shock wave, and then the flow undertakes turn in the scramjet inlet The flow behind the conical shock was calculated using the oblique shock relationship, which is a fairly good approximation for the conical shock at stations far from the base body surface.

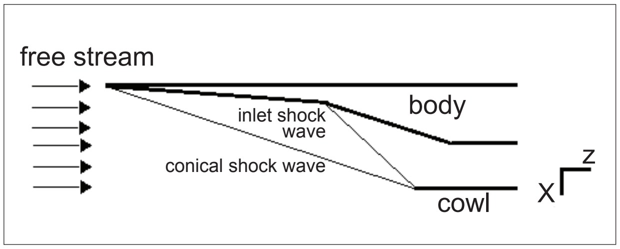

Figure 8. Scheme for the flow on the compression surface.

The results are shown in Fig. 9. As one can see, as the ramp angle increases, the maximum allowed altitude increases while the minimum increases also, the operating corridor (upper minus lower limits) remains quite constant of the order of 10 km. As a design option, we chose an operating altitude range of 40 to 50 km. Consequently, the ramp shock wave angle was found to be 25°, and the ramp angle was calculated giving 20° with respect to the z-axis.

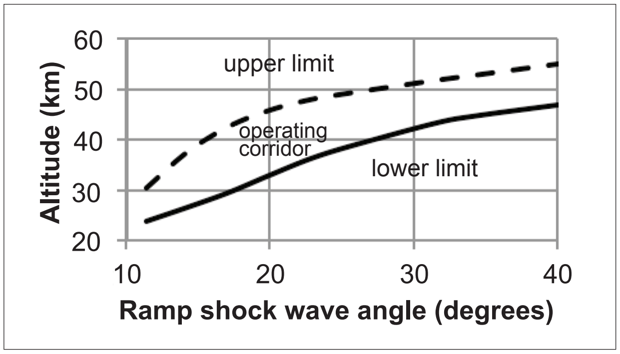

Figure 9. Relationship between the secondary-shock wave angle and the required altitude limits. According to the International Standard Atmosphere model.

c) Combustor and nozzle

Although the combustor and expansion systems were not the aim of the work presented here, a 108 mm x 270 mm long flat surface and a 115 mm long constant slope ramp of 15° were integrated to the compression surface.

d) Final configuration

The model tested in the T3 tunnel is shown in Fig. 10. In this figure one can see the location of a set of 7 piezoelectric pressure transducers used to assess the pressure field on the compression surface. The 781 mm x 327.5 mm model was machined with a CNC milling machine and made by stain less steel, Fig. 11 shows photographs of the actual model.

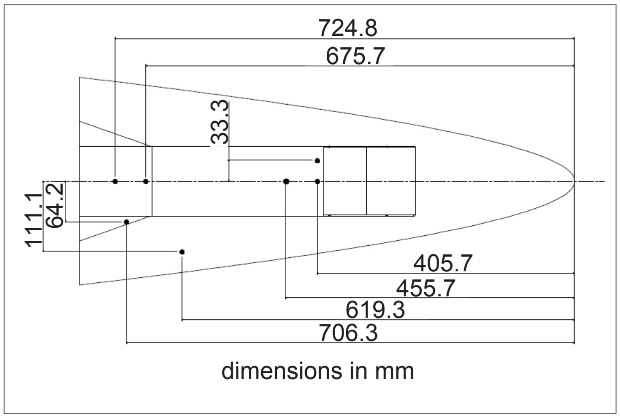

Figure 10: Location of pressure transducers.

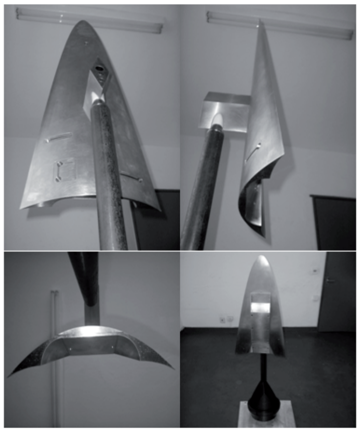

Figure 11: Actual machined model.

EXPERIMENTAL WORK

a) T3 shock tunnel facility

The large stagnation enthalpy and pressure required for simulation of hypersonic flow make the shock tunnel facilities the only applicable tools for this purpose. The shock tunnel consists of a high pressure section (driver section) separated by means of a diaphragm section from a low pressure section (driven section). When the diaphragm bursts a shock wave propagates toward the driven, while an expansion wave propagates into the driver. The shock wave interacts with the cold air in the driven section, increasing pressure and temperature. Once the shock wave reaches the nozzle diaphragm, it is reflected and interacts with the contact surface – the interface between the gases. After few interactions and reflections, the resulting high temperature and high pressure are used as stagnation conditions for the supersonic nozzle located at the end of the driven section.

The hypersonic shock tunnel T3 was used in the present work. This shock tunnel is located at the Laboratory Prof. Henry. T. Nagamatsu of Institute for Advanced Studies (IEAv) from Department of Science and Aerospace Technology (DCTA). That hypersonic facility comprises of two other shock tunnels T2 and T1, 11.50 m and 7.80 m long, respectively. The T3 is 17.50 m long with a test section diameter of 610 mm.

The T3 has a moveable sting aligned with the nozzle axis that permits an easy longitudinal alignment of the models; a commercial masonry level is generally used for lateral alignment.

b) Test campaign

The test conditions were controlled by the driver to-driven pressure ratio along with the driver gas choice (Helium or dry air). That is because Helium produces higher stagnation enthalpies than air. The Mach number of 10 was fixed by the nozzle geometry. The test matrix is shown in Table 1. Piezoelectric pressure transducers were used for measuring the reservoir pressure and the incident shock wave speed in driven section. These data were used to estimate the total temperature and free stream conditions. The last four runs, with lower Mach numbers, were made with the model inside the nozzle, in order to better visualize the flow at the inlet.

c) Airflow visualization

As shown in Table.1, the free stream static temperature varied from 38 to 122K and static pressure from 0.13 to 0.89kPa. The Reynolds number ranged between 2.25 x 10^6 to 8.76 x 10^6 (m^{-1}). These Reynolds numbers indicates that the flow is laminar over a considerable distance from the leading edge of the model. Furthermore, the low Knudsen numbers suggest continuum flow conditions to be expected throughout the investigated model, except inside the slip region.

Although the forebody compression surface presents some longitudinal angle variation, detailed observation of the model sketches can show that air flow turning is so slight – in fact the turning angle reaches 3° as a maximum before the inlet – that the flow in this region can be compared with the flow over a flat plate under the same conditions. Several works (Nagamatsu, et al., 1961; Nagamatsu, et al., 1960; Hayes, et al., 1959) have shown the existence of the three different flow field regions downstream the leading edge of a

Table 1. Test matrix.

Stagnation conditions		**Freestream conditions**				
Pressure (MPa)	**Temperature (K)**	**Static pressure (kPa)**	**Static temperature (K)**	**Mach Number (M)**	**Reynolds Number (Re)(m^{-1})**	**Knundsen Number (km)**
15.0	2150	0.30	121.0	10.0	2.25×10^6	0.19
18.2	1624	0.35	87.9	10.0	4.36×10^6	0.11
16.0	1535	0.31	82.5	10.0	4.20×10^6	0.12
18.2	1820	0.48	109.2	9.4	3.96×10^6	0.11
20.3	1558	0.48	87.9	9.6	5.73×10^6	0.08
5.3	795	0.17	41.6	9.7	7.03×10^6	0.11
5.4	715	0.19	38.0	9.6	8.76×10^6	0.09
5.0	834	0.13	41.3	10	5.58×10^6	0.15
20.3	1706	0.40	92.8	10.0	4.48×10^6	0.11
20.0	1840	0.74	122	8.9	4.91×10^6	0.08
19.1	1730	0.12	114.3	8.9	5.35×10^6	0.07
20.3	1757	0.11	114.8	9.0	5.41×10^6	0.07
19.6	1702	0.13	116.9	8.7	6.17×10^6	0.06

flat plate. The three distinct flow regions are the slip region, the strong and weak interaction regions (Toro, et al., 1998).

Even under continuum flow conditions (kn<<1) the existence of slip near leading edge for very large Mach numbers was reported elsewhere (Nagamatsu, et al., 1961). According to the theory developed by those authors, the length of the slip region can be assumed as proportional to the free stream Mach number. Indeed, following the same procedure as taken by Minucci (Minucci, 1991) it was possible to estimate the slip region length as between 0.03 and 0.1 mm. In this region, which can be considered a rarefied flow, the Boltzmann equations are more suitable. As it can be noted in the schlieren photograph in Fig. 12, the flow pattern around the leading edge no longer presents a bow shock as in the continuum case, instead, near the leading edge the shock wave starting point was almost imperceptible, a main characteristic of a slip condition.

Figure 12: Mach 10 flow past the model leading edge. Reservoir conditions: 20.3 MPa and 1706 K.

Furthermore, the region that follows the slip region presents shock-wave/boundary-layer interactions, the extent of the influence of this region downstream depends on the size of the subsonic portion of the boundary layer and on the strength of the shock wave (Bertin, 1994). When the rate of growth of the boundary layer is large, the boundary layer and the shock wave are merged within a limited region. In this situation, the outer inviscid flow is strongly affected by the displacement thickness, which in turn substantially affects the boundary layer. This mutual process is called strong viscous interaction (Anderson, 1989).

As stated before, due to the low Reynolds number, one can assume that the boundary layer is laminar. The similarity parameter that governs laminar viscous interactions is given by:

$$\bar{\chi} = \frac{M_\infty^3}{\sqrt{Re_z}}\sqrt{\frac{\mu_w \rho_w}{\mu_e \rho_e}} \qquad (16)$$

Re_z is based on the free stream properties, calculated at a distance z from the leading edge. While M_∞ is the free stream Mach number, μ is the dynamic viscosity ρ is the density and the subscript *w* relates to the wall and *e* to the edge of the boundary layer, respectively. The effects of the hypersonic viscous interactions on the pressure distribution over a flat plate as function of the parameter $\bar{\chi}$ were presented in several works (Nagamatsu, et al., 1961; Hayes, et al., 1959; Minucci, 1991; Anderson, 1989). A common result is that the induced pressure change varies linearly with $\bar{\chi}$ .Thus, one can write:

$$\frac{\Delta p}{p_\infty} = F \cdot \bar{\chi} \qquad (17)$$

where:

ρ is the static pressure;

Δρ is the static pressure perturbation;

F is a function of the ratio of the specific heats and the wall temperature condition.

Another important result relates the leading-edge shock-wave angle β with the local Reynolds number inside the strong interaction region as below:

$$\beta \cong \frac{d\delta^*}{dz} \propto \left[\left(\frac{\mu_w \rho_w}{\mu_e \rho_e} \right) / Re_z \right]^{1/4} \sqrt{M_\infty} \qquad (18)$$

where δ* is the displacement thickness.

Following, in the weak interaction region, the displacement effects are small enough so the inviscid flow does not interact with the boundary layer. Also, small pressure gradients inside the boundary layer permit the use of the Blausius solution for a viscous flow over a flat plate, adapted for compressible flows. Thus, the displacement thickness variation with the local Reynolds number within the weak interaction region is so as (Anderson, 1991):

$$\frac{d\delta^*}{dz} = G \frac{0.86}{\sqrt{Re_z}} \qquad (19)$$

where G accounts for the compressibility effects, but also it is a function of M_∞, the wall temperature, the Prandtl number and the boundary-layer-edge temperature.

After careful data analysis of a high definition version of Fig.12, the shock wave angle was measured using a computational grid on the image, thus its dependence on the viscous interaction parameter was investigated. The results are shown in Fig.13. It is evident that the curve follows the same pattern as seen in a strong interaction region at foremost stations. In fact, as previously stated, the small shock-wave angle and the low Reynolds number imply a merged shock-wave/boundary-layer. Moreover, the measured angles were quite larger than the predicted by the inviscid, calorically perfect theory (with ratio of specific heats, γ = 1.4). This result is reasonable since the displacement thickness δ* modifies the effective body; the effect is exacerbated by the adverse pressure gradient due to the slight turning of the flow along the forebody region. Besides, the author believes that the nozzle's non-equilibrium effects certainly impart some deviations from the calculated inviscid value at stations far from the strong interaction zone, since γ must be considered a function of the local pressure and temperature.

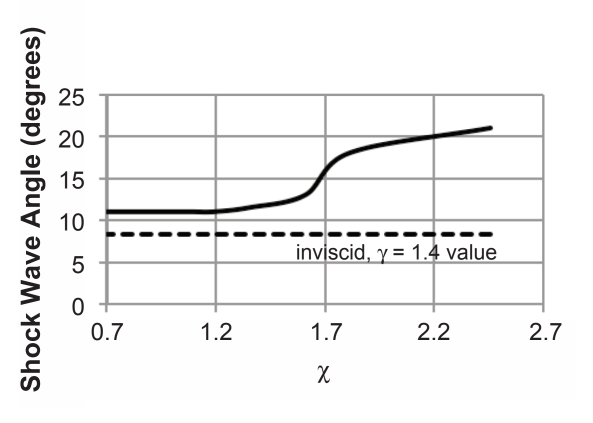

Figure 13: Primary shock wave angle variation with the parameter $\chi = \bar{\chi} / \sqrt{\frac{\mu_w \rho_w}{\mu_e \rho_e}}$. Same flow conditions indicated in Fig. 12.

Another aspect of the hypersonic flow which was observed concerns the flow profile over the inlet ramp. Like the flow over a flat plate, the shock-wave/boundary-layer interaction depends largely on the length of the subsonic portion of the boundary layer and on the shock wave strength. The adverse pressure gradient causes the boundary layer to thicken as it approaches the ramp deflection. If the conditions are such that the boundary-layer separates, as depicted in Fig. 14, a series of compression waves is formed in the separation point and they coalesce into a single curved shock-wave. Downstream that point, the region of separated flow features unsteady nature and large gradients. In the reattachment point, the inviscid flow along the effective ramp encounters the actual ramp, a phenomenon which causes an incremental compressive turning. The compression waves formed in the reattachment point coalesce to another shock wave. Finally, the separation and the recompression shock waves interact downstream. In this model, the inviscid flow impinges two successive compression ramps, the

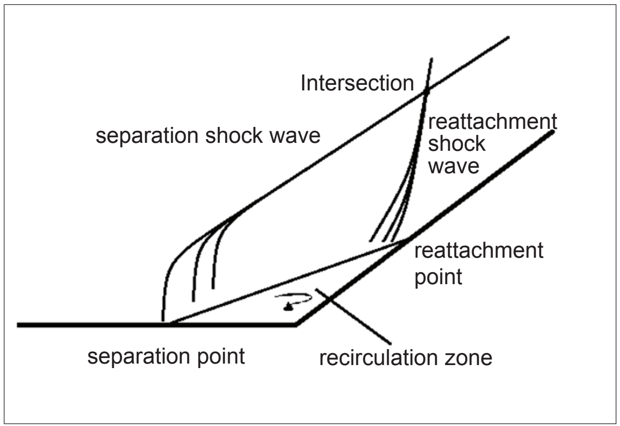

Figure 14: Main characteristics of a separated flow over a compression ramp. Adapted (Bertin, 1994).

first one represents the separated region and the second one the region of reattached flow. Occasionally, the shock waves intersect at some point.

Figure 15 shows a schlieren photograph of the flow over the rear region of the compressive ramp. With the fins mounted, the complete flow development over the inlet ramp could not be observed. However, the coalescent compression waves, that seem to intersect downstream the frame region, can be seen. Their extensions indicate a large separated region compared with the ramp length. In addition to that, it was possible to infer the angle of its linear portion as being 27°, only 8% larger than the inviscid, calorically perfect value, 25°.

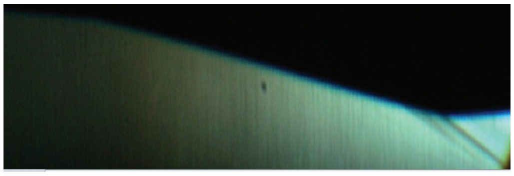

Figure 15. Mach 8.7 flow past the inlet ramp. Reservoir conditions: $P_0 = 19.6$ MPa , $T_0 = 1702$ K.

d) Static pressure measurements

One can see in Fig. 16 the static pressure variation with the distance from the nose leading edge along the centerline of the model during the first three tests. The correspondent parameter $M_\infty^3/\sqrt{Re_\infty}$ was indicated in that figure. The inviscid solution for the pressure distribution over the pure waverider surface was also inserted. Regarding that figure it was found that the pressure decreases from $z/L_w = 0.52$ to 0.58, just after the compression ramp. This result is believed to be consequence of the existence of a non-centered expansion fan formed at the end of the ramp, caused by a separated region. Thus, where the flow is believed to be fully expanded, such as at station $z/L_w = 0.58$, the pressure is slightly lower than at the initial part of the expansion fan, $z/L_w = 0.52$.

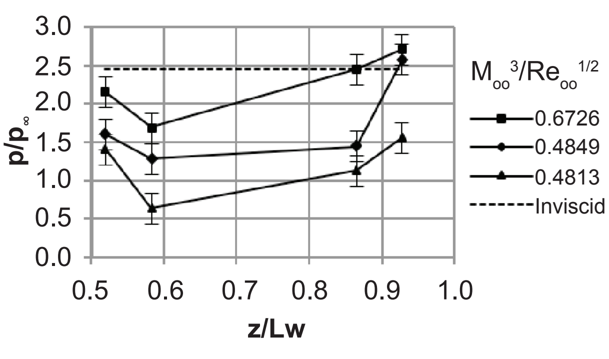

Figure 16. Pressure distribution along the model center line. L_w is the model length.`

Furthermore, in Fig. 16, from stations $z/L_w = 0.58$ to 0.86, there is a pressure increase despite the fact that station $z/L_w = 0.86$ was situated over the expansion ramp. Although a more complete pressure survey is needed, it is believed that flow separation is also possible to take place on the flat portions between stations $z/L_w = 0.58$ and $z/L_w = 0.86$, since the boundary layer thickness is increasing along the model length. Thus, it is entirely possible that a "bubble" shaped shock forms between these stations (Bertin, 1994). Also, from stations $z/L_w = 0.86$ to 0.93, located over the expansion ramp, a pressure increase can be noted, probably indicating that at the nozzle the flow separation and reattachment occur before point $z/L_w = 0.93$.

CONCLUSIONS

An experimental investigation of a 781mm waverider model was performed at the Laboratory Prof. Henry. T. Nagamatsu/IEAv/DCTA. Schlieren photographs and static pressure measurements were made for further flow analysis. The waverider surface was constructed according to the Hypersonic Small Disturbances Theory (Rasmussen, et al., 1990), scramjet compression and expansions ramps were integrated to the pure waverider surface.

The stagnation conditions as well as the free stream properties were estimated using the numerical codes. The tunnel operated at Mach number ranges of 8.9 to 10, Re = 2.25 x 10^6 to 8.76 x 10^6 (m^{-1}) and Kn = 0.06 to 0.19.

As results, the schlieren photographs demonstrated the attached shock wave, a key fact of the waverider concept, and the formation of the compression waves in the inlet region.

Furthermore, the pressure distribution over the compression surface was measured. The pressure rise found downstream the centerline is believed to have been caused by the boundary layer thickness increase and consequently flow separation. However, it's believed that the entire flow complexity was not properly depicted by this investigation and shall be subject of future works.

ACKNOWLEDGEMENTS

The authors hereby express their gratitude to: Agência Espacial Brasileira (AEB), Conselho Nacional de Desenvolvimento Científico e Tecnológico (CNPq), Coordenação de Aperfeiçoamento de Pessoal de Nível Superior (Capes), Fundação de Amparo à Pesquisa do Estado de São Paulo (Fapesp), and Financiadora de Estudos e Projetos (Finep).

REFERENCES

Anderson, J. D., 1991, "Fundamentals of Aerodynamics", New York , MacGraw-Hill, 2nd Edition.

Anderson, J. D., 1989, "Hypersonic and High Temperature Gas Dynamics", New York , McGraw-Hill.

Bertin, J. J., 1994, "Hypersonic Aerothermodynamics", New York, AIAA Education Series.

Hayes, W. D. and Probstein, R. F., 1959, "Hypersonic Flow Theory", New York, Academic Press.

Heiser, W. H., et al., 1994, "Hypersonic Airbreathing Propulsion", AIAA Education Series.

Javaid, K. H., Serghides, V. C., 2005, "Airframe Propulsion Integration Methodology for Waverider Derived Hypersonic Cruise Aircraft Design Concepts", Journal of Spacecraft and Rockets, AIAA, No. 5 , Vol. 42. , pp. 663-671.

Kim, B. S., Rasmussen, M. L., Jischke, M. S., 1983, "Optimization of Waverider Configurations Generated from Axisymmetric Conical Flows" Journal of Spacecraft, AIAA, No. 5 , Vol. 20. , pp. 461-469.

Minucci, M. A. S., 1991, "Experimental Investigation of 2-D Scramjet Inlet at Flow Mach Numbers 8 to 25 and Stagnation Temperature of 800K to 4100K", Ph.D. dissertation, Aeronautical Engineering Dept. Ressenlaer Polytechnique Institute, Troy, NY.

Nagamatsu, H. T., Sheer, R. E. Jr, 1961, "Hypersonic Shock Wave-Boundary layer Interaction and Leading Edge Slip", American Rocket Society Journal, No. 5, Vol. 30, pp. 454-462.

Nagamatsu, H.T., Li., T. Y., 1960, "Hypersonic Viscous Flow Near the Leading Edge of a Flat Plate" Physics of Fluid., No. 1, Vol. 3, pp. 140-141.

Nonweiler, T. R. F., 1963, "Delta wings of Shape Amenable to Exact Shock Wave Theory", Journal of the Royal Aeronautical Society, Vol. 67, p. 39.

O'neill, M. K., Lewis, M. D., 1992, "Optimized Scramjet Integration on a Waverider", Journal of Aircraft, AIAA, No. 6 , Vol. 29, pp. 1114-1121.

Rasmussen, M. L., He, X., 1990, "Analysis of Cone-Derived Waveriders by Hypersonic Small-Disturbance Theory", Proceedings of the First International Hypersonic Waverider Symposium.

Rault, D. F. G., 1994, "Aerodynamic Characteristics of Hypersonic Viscous Optimized Waverider at High Altitudes", Journal of Spacecraft and Rockets, No. 5, Vol. 31, pp. 719-727.

Toro, P. G. P., et al, 1998, "Hypersonic Flow Over a Flat Plate", 36th AIAA Aerospace Sciences Meeting and Exhibit, Reno, NV.

Wang, Y., Zhang, D., Deng, X., 2007, "Design of Waverider Configuration with High Lift-Drag Ratio" Journal of Aircraft, No. 1, Vol. 44, pp. 144-148.